GLOBAL MHD SIMULATIONS OF THE DYNAMICS OF THE MAGNETOSPHERE: WEAK AND STRONG SOLAR WIND FORCING

Joachim Raeder

Institute of Geophysics and Planetary Physics, UCLA, Los Angeles, California 90024-1567

Abstract

We present results from two global MHD simulation runs that use the same IMF sequence but different plasma parameters. The IMF is first taken to be predominantly northward and causes the magnetosphere to enter a quiet state. After that a 5 hour long period of steady southward IMF is used. We compare the two simulation runs on the basis of their computed AL and AU indices and their signatures in the near-Earth and the distant tail. In the case with strong solar wind forcing we find the signatures of three substorms following the southward turning of the IMF. With each of these substorms, the computed AL index (AL_s) decreases rapidly, in the near-Earth tail the field dipolarizes, the temperature increases and earthward flows develop. In the distant tail we find the signatures of plasmoids associated with the substorms. In the weakly forced case we find substorm signatures in AL_s, but signatures in the tail are very weak or absent. In both cases the geomagnetic activity is partly driven and partly spontaneous.

1. Introduction

Considerable evidence has been accumulated over the past few decades that magnetospheric activity is intimately controlled by the solar wind impinging onto the Earth's magnetosphere. However, the interaction of the magnetosphere with the solar wind is by no means a simple one. Many studies have been conducted to establish a relationship between geomagnetic activity and various solar wind parameters (see Baker et al. [1984] for an overview). However, there does not seem to be a one to one relationship between any of the solar wind parameters that have been considered and the common measures of geomagnetic activity, such as the AL or Dst indices. More recent studies have produced evidence that two different "modes" may contribute to geomagnetic activity. While one part of the activity may be described as being directly driven by the solar wind, another part is only indirectly controlled by the solar wind and may be attributed to an intrinsic instability in the geomagnetic tail [Baker et al., 1984; Bargatze et al., 1985].

One of the most common and prominent manifestations of geomagnetic activity is the auroral (or geomagnetic) substorm. The most widely accepted model for substorms relates their occurrence to a negative B_z component of the IMF which is thought to "load" the tail first by reconnecting solar wind magnetic field at the dayside magnetopause, and transferring magnetic flux into the tail lobes. Subsequently, as the tail accumulates more and more magnetic flux (and thus energy), the tail becomes unstable, develops a near-Earth X-line, and releases the excess energy. Part of that energy is released in form of a plasmoid that is ejected tailward, while another part is dissipated both in the tail and in the ionosphere [e.g. McPherron, 1990].

Many of the predictions of this model have been confirmed by observations. In particular, an association between tailward propagating plasmoids in the tail with substorm onsets has been found [Slavin et al., 1992; Moldwin and Hughes, 1993] which implies that substorms are indeed closely related to a reconnection process in the tail.

Other observations cannot be easily explained by the near-Earth X-line model. Among these is the dynamics of the near-Earth tail, at or just beyond geosynchronous orbit, which is closely related to the onset of the expansion phase of a substorm [Takahashi et al., 1987; Lui et al., 1988; Lopez and Lui, 1990; Ohtani et al., 1992]. Also, the initial signature of the auroral substorm, the brightening of the most equatorward arc, seems to map magnetically into the near-Earth plasma sheet [Lopez et al., 1990]. Reconnection is very unlikely to occur so close to the Earth, so other mechanisms must be invoked to explain these observations. One more puzzling fact is the existence of steady magnetospheric convection events (also called "convection bays"). During these events, the IMF B_z is southward and steady for a time period that is much longer than the typical substorm recurrence time of 2 to 3 hours [Borovski et al., 1993], yet no substorm signatures are apparent [Pytte et al., 1978; Segeev and Lennartson, 1988; Yahnin et al., 1994]. Instead, the magnetosphere exhibits a state of enhanced convection with intensified auroral electrojets and a substorm-like AL index.

Because of these difficulties a number of other substorm models have been proposed; however, none of them can explain all of the observations (for recent reviews see McPherron [1990] or Fairfield [1992]).

In this study we use global MHD simulations to examine the relation between the solar wind and geomagnetic activity for two simple cases. Global MHD simulations have been used in the past to study a variety of magnetospheric processes [eg. Brecht et al., 1982; Ogino, 1986; Fedder and Lyon, 1987; Watanabe and Sato, 1990; Walker et al., 1993]. Assuming that the MHD description is valid throughout the magnetosphere, and that all the relevant boundary conditions are sufficiently well known and properly specified, a global MHD model should be able to elucidate the principal physical processes that lead to geomagnetic activity. However, in practice this task is very difficult to achieve due to a number of factors. First, the (ideal) MHD description is not valid everywhere, in particular at boundary layers, thin current sheets and in the low β regions near the Earth, such as the radiation belts and the ring current. Some of these limitations can be overcome by including properly specified dissipation terms (see below). Secondly, the ionospheric boundary is very complicated and allows for the exchange of mass, momentum, energy, and electrical current with the magnetosphere. Many of the earlier model had considerably simplified this boundary because of computational constraints. The model that we use for this study includes a self-consistent model of the ionosphere and its coupling with the magnetosphere. The ionosphere model not only provides the necessary closure of the Birkeland current systems, but also allows us to study other ionospheric parameters that are related to geomagnetic activity. In particular, we can derive quantities that are typically observed from the ground, such as the magnetic field perturbations and the AL/AU indices.

The remainder of the paper is organized as follows. In the next section we will give a short overview of the model and the parameters used for this study. We will then present two simulation runs with the same IMF but different solar wind plasma parameters and discuss the principal features of geomagnetic activity on the ground and in the tail. In the last section we will summarize our results.

2. The Model

For this study we use a global MHD code which also includes an ionospheric model for the closure of field aligned currents. In order to accommodate the large simulation volume with a 250 R_E tail and long simulation times together with good resolution, the simulation code was parallelized for MIMD (Multiple Instruction - Multiple Data) machines by using a domain decomposition technique. The model solves the ideal MHD equations for the magnetosphere and a potential equation for the ionosphere. However, because of numerical effects, diffusion and resistive effects occur in the MHD solutions; these permit viscous interactions and also magnetic field reconnection to a limited extent. In some cases the numerical resistivity is too low to allow for adequate reconnection rates. For this reason we have also included a resistive term into Ohm's law which is based on the resistivity model described below.

The magnetospheric (MHD) part of the model is solved by a finite difference method which is conservative for the gas-dynamic part of the MHD equations:

$$\frac{\partial \rho}{\partial t} = -\underline{\nabla} \cdot (\rho \underline{\mathbf{v}})$$

$$\frac{\partial \rho \underline{\mathbf{v}}}{\partial t} = -\underline{\nabla} \cdot (\rho \underline{\mathbf{v}}\underline{\mathbf{v}} + p) + \underline{\mathbf{j}} \times \underline{\mathbf{B}}$$

$$\frac{\partial e}{\partial t} = -\underline{\nabla} \cdot (\{e + p\}\underline{\mathbf{v}}) + \underline{\mathbf{j}} \cdot \underline{\mathbf{E}}$$

$$\frac{\partial \underline{\mathbf{B}}}{\partial t} = -\underline{\nabla} \times \underline{\mathbf{E}}$$

$$\underline{\nabla} \cdot \underline{\mathbf{B}} = 0$$

$$\underline{\mathbf{E}} = -\underline{\mathbf{v}} \times \underline{\mathbf{B}} + \eta \underline{\mathbf{j}}$$

$$\underline{\mathbf{j}} = \underline{\nabla} \times \underline{\mathbf{B}}$$

$$e = \frac{1}{2}\rho v^2 + \frac{p}{\gamma - 1}$$

The $\underline{\mathbf{j}} \times \underline{\mathbf{B}}$ and $\underline{\mathbf{E}} \cdot \underline{\mathbf{j}}$ terms are treated as source terms because of the very low plasma β, and the large magnetic field gradients near the Earth do not allow the use of the full conservative form of the MHD equations. The numerical scheme has very low numerical dissipation. In order to allow for magnetic merging we include a resistive term in Ohm's law. The resistivity is a nonlinear function of the local magnetic field gradients. It takes essentially the form:

$$\eta = \alpha {j_1}^2$$

with

$$j_1 = \begin{cases} j_2 & \text{if } j_2 \geq \delta \\ 0 & \text{else} \end{cases}$$

and

$$j_2 = \frac{|j|\Delta}{|B| + \epsilon}$$

where j is the local current density, B the local magnetic field, Δ is the gridspacing, and ϵ is a very small number to avoid division by zero. j_2 is a normalized current ($0 \leq j_2 \leq 1$) that is used as a switch for the resistivity. In places where the resistivity is switched on it becomes proportional to the square of the local current. Similar resistivity models have been used in the past to model the kinetic effects that lead to anomalous resistivity [Hoshino and Nishida, 1983]. The parameters α and δ determine the value of the resistivity and the current threshold that must be reached for the resistivity to be switched on. These parameters are choosen such that the resistivity η is nonzero only at very few gridpoints in strong current sheets.

The numerical grid is rectangular and nonuniform with the highest spatial resolution near the Earth (about 0.5 R_E). It extends 30 R_E in the sunward direction, 250 R_E in the tailward direction and 70 R_E in the Y and Z directions. The gas-dynamic part of the equations is spatially differenced by using a technique in which fourth order fluxes are hybridized with first order (Rusanov) fluxes [Harten and Zwas, 1972; Hirsch, 1990]. The magnetic induction equation is treated differently to ensure $\nabla \cdot \mathbf{B} = 0$ by following a method outlined by Evans and Hawley [1988] that conserves $\nabla \cdot \mathbf{B}$ exactly. The time stepping scheme for all variables consists of a low order predictor with a time centered corrector, which

is second order accurate in time. The outer boundary conditions are fixed at the given solar wind values on the upstream side. At the other boundaries we apply open, i.e., zero normal derivative, boundary conditions.

The inner boundary, where the MHD quantities are connected to the ionosphere, is taken to be a shell of radius 3.7 R_E centered on the Earth. The choice of this radius is a compromise and necessitated by numerical considerations, such as extraneously high Alfvén speeds and very large magnetic field gradients closer to the Earth. However, the choice allows for the proper mapping of all relevant field aligned current systems. Inside this shell we do not solve the MHD equations, but assume a static dipole field. The important physical processes within the shell are the flow of field aligned currents (FACs) and the closure of these currents in the ionosphere. At each time step we map the magnetospheric FACs from the 3.7 R_E shell onto the polar cap using a static dipole field. We then use the FACs as input for the ionospheric potential equation:

$$\underline{\nabla} \cdot \underline{\underline{\Sigma}} \cdot \underline{\nabla}\Phi = -j_{\parallel} \sin I$$

which is solved on the surface of a sphere with a radius 1 R_E. Here Φ denotes the ionospheric potential, $\underline{\underline{\Sigma}}$ is the tensor of the ionospheric conductance, $j_{\parallel}$ is the mapped FAC with the downward current considered positive and corrected for flux tube convergence, and I is the inclination of the dipole field at the ionosphere. The boundary condition $\Phi = 0$ is applied at the equator. For the ionospheric Hall and Pedersen conductances, Σ_H and Σ_P, which enter the conductance tensor $\underline{\underline{\Sigma}}$ [see e.g., Kamide and Matsushita, 1979] three ionization sources are taken into account. First, for the solar EUV ionization we use the model of Moen and Brekke [1993]. Second, we compute the mean energy and energy flux of precipitating electrons associated with upward FACs using the relationship developed by Lyons et al. [1979]. Third, diffuse electron precipitation is modeled by assuming complete pitch angle scattering of electrons at 3.7 R_E. The conductances are then computed from the electron precipitation parameters using the empirical relations of Hardy et al. [1987]. Using the mapped FACs and the ionospheric conductances the potential equation is solved, and the the ionospheric potential is mapped to the 3.7 R_E shell where it used as a boundary condition for the magnetospheric flow by taking $\underline{v} = (-\underline{\nabla}\Phi) \times \underline{B}/B^2$.

From the ionosphere model we get the FACs and the conductances as the principal prognostic variables (in meteorological parlance). From these we derive a set of diagnostic variables that are more commonly observed. First, we determine the total ionospheric current I_t. We calculate the equivalent (poloidal) ionospheric current by subtracting the irrotational part of I_t [eg. Kamide, 1982]. From the equivalent current we find the ground magnetic perturbation for a large number of "ground stations" (every 15^0 in longitude and every 1^0 in latitude), assuming that the equivalent currents flow at an altitude of 110 km. Combining all ground stations between latitudes of 65^0 and 75^0 we compute "ideal" AL and AU indices, which we call AL_s and AU_s in the following to distinguish them from the actual AL and AU indices.

The initial conditions for the magnetic field are constructed from the superposition of the Earth's dipole over a mirror dipole, such that B_x vanishes at $x = 16\ R_E$. Sunward of the plane of symmetry at 16 R_E the field is replaced by the initial solar wind field. This procedure ensures a divergence-free transition from the constant solar wind field to the Earth's dipole field. The simulation box is initially filled with tenuous (0.1 cm^{-3}) and cold (5000^0 K) plasma of zero velocity. The solar wind flow is switched on at the sunward boundary at time t=0. We first let the system evolve under southward IMF conditions for 90 min, which is somewhat more than is required for the solar wind to pass once through the simulation box. By comparing runs with different initial conditions we found that the specific initial conditions have only a minimal effect on the structure of the magnetosphere after the solar wind with southward IMF

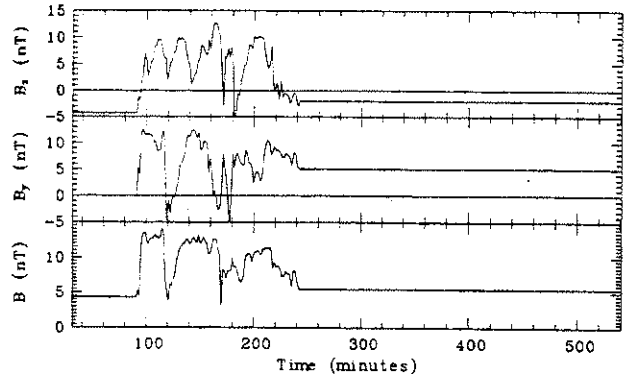

Fig. 1. IMF input data used for the simulation runs. B_x is zero and the plasma parameters are given in the text.

has passed once through the simulation box. The southward IMF conditions let a neutral line (at about x = -25 R_E) and fast tailward flows to evolve, which clear the tail of any structures that are there as a result of the initial conditions. After this initial phase we use IMP 8 B_y and B_z time series for the next 150 minutes with a resolution of 2 min as boundary conditions on the sunward side (see Fig. 1). During this time interval the IMF is very variable, but mainly northward with a strong positive B_y component. This IMF sequence brings the magnetosphere into a quiet state. At t=225 min the field turns southward, and after t=240 min the field is kept at B_z=-2nT and B_y=5nT. The two runs that we present in this paper differ only in their solar wind plasma parameters. The solar wind density, velocity and pressure are (13 cm^{-3}, 500 km s^{-1}, 54 picoPascal) for run #1 and (6 cm^{-3}, 350 km s^{-1}, 10 picoPascal) for run #2, respectively.

3. Results

Figures 2 and 3 display the AL_s and AU_s indices for run #1 (strong forcing) and run #2 (weak forcing), respectively. We will not discuss the first 150 minutes because they are dominated by the startup phase of the simulation and the following northward turning of the IMF. Between 150 min and 225 min the IMF is predominantly northward with a strong B_y component. During this time the AU_s and AL_s indices of run #2 are very quiet and do not indicate any geomagnetic activity. The AL_s index stays near -50 nT, which may be regarded as its quiet time value. Similarly,

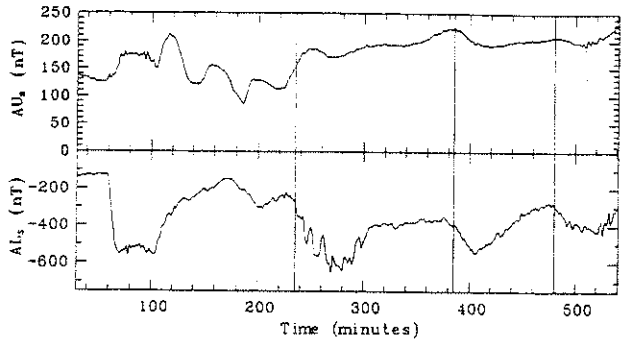

Fig. 2. The computed AU_s and AL_s indices from run #1 (strong solar wind forcing).

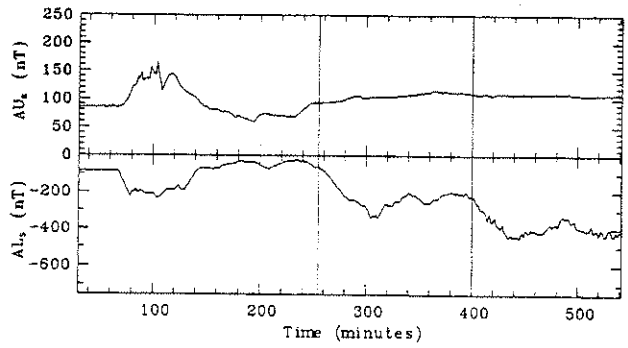

Fig. 3. The computed AU_s and AL_s indices from run #2 (weak solar wind forcing).

the AU_s index shows little variation and stays between 50 and 100 nT. The indices of run #1 do not show a quiet magnetosphere, but rather indicate some moderate activity. This higher activity is obviously related to the higher solar wind dynamic pressure (by a factor of 4.4) and two brief southward excursions of the IMF at 170 min and 180 min. The decrease in the AL_s index beginning at 175 min in run #1 may indicate that a small substorm is associated with these IMF southward excursions. Because this event is fairly small we will not analyze it in detail here. However, it is interesting to note that there is no corresponding feature in the AL_s index of run #2. This may indicate that there is some threshold that must be exceeded to cause a substorm. It seems that this threshold was exceeded in run #2, but not in run #1.

At 225 min the field turns southward at the dayside magnetopause. In the strongly forced case, run #1, the AL_s and AU_s indices react very quickly to this change in the solar wind parameters. The AU_s index starts to rise at the same time as the IMF turns southward at the magnetopause. However, this change looks similar to changes that occurred during the northward IMF interval and may have nothing to do with the southward turning of the IMF. The same argument holds for the small drop in the AL_s index that begins at 225 min. Ten minutes later, at 235 min, the AL_s index begins to drop sharply. Obviously, this sharp drop and the following stepwise decrease with intermittent short recoveries indicates an expansion phase of a substorm. The AL_s index reaches a minimum of about -600 nT at 275 min, 30 min after the onset. The AL_s index then recovers to about -400 nT 40 minutes later.

In the case of weak forcing (run #2) the sequence of events is similar but the signatures are much weaker and occur later. The AU_s index starts to rise about 10 minutes after the southward turning of the IMF. There are no significant variations in the AL_s index until about 30 minutes after the southward turning of the IMF. The ensuing substorm expansion phase is smoother and lasts longer than in the previous case (50 minutes versus 30 minutes), although the decrease in the AL_s index is only moderatly smaller (300 nT versus 400 nT).

In both cases the AL_s index does not fully recover to the pre-onset level. This can be attributed to the fact that the IMF remains unchanged in its southward direction and continues to drive the magnetosphere. The AL_s index stays relatively flat in both cases for about 80 minutes until it drops again. The decrease is similar in both cases (about 200 nT) but occurs faster in the strongly forced case (25 minutes versus 35 minutes). These drops, together with their respective recoveries may be regarded as small substorms, although they start from an already enhanced AL_s index level. In both cases there seems to be another small substorm later on in the simulation run; however, the recoveries are not fully encompassed in the simulations and we therefore do not discuss them here.

In order to study the dynamic changes in the tail and how they are related to the magnetic indices we use "virtual spacecraft", i.e., we look at time series of the MHD quantities at certain locations within the tail.

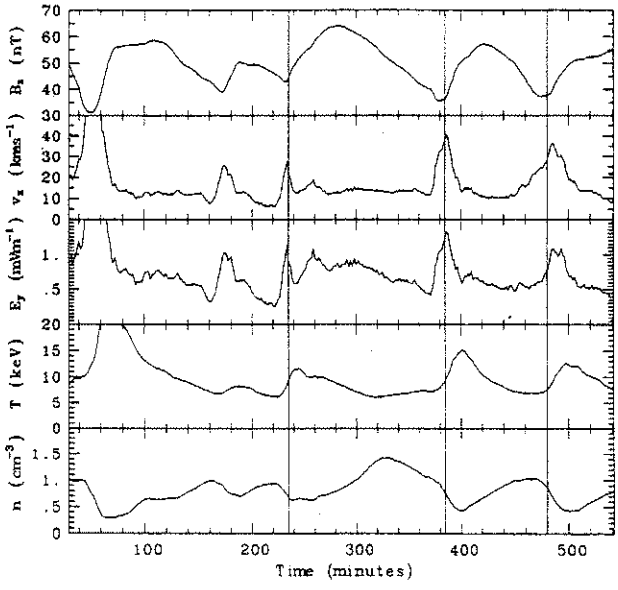

Fig. 4. Time series ("virtual spacecraft observation") of B_z, v_x, E_y, temperature, and number density at (-8 R_E,0 R_E, 0 R_E) for run #1.

Figure 4 shows the z-component of the magnetic field (B_z), the x-component of the velocity (v_x), the y-component of the electric field (E_y), the temperature, and the number density for run #1 at (-8 R_E, 0 R_E, 0 R_E) as functions of time.

The total magnetic field (not shown here) is almost identical to B_z. Within a few minutes of the AL_s index onset times (at 235 min, 385 min, and 480 min) typical substorm features become apparent in the near-Earth tail. First, B_z starts to increase, i.e. the near-Earth tail field dipolarizes, at the same time as the AL_s index begins its steep decrease. Also, the temperature begins to rise by about a factor of two in all three of the substorms. At the same time when the temperature increases, v_x reaches a maximum of about 30 km s^{-1}, which shows either that more energetic plasma is transported earthward, or that the plasma is adiabatically compressed and heated. Both processes probably play a role here, because the number density is almost inversely correlated with the temperature, which precludes an entirely adiabatic process, and the field magnitude increases, which implies adiabatic compression. The temperature increases may be regarded as an MHD type signature of particle injection into the inner magnetosphere. Although the MHD description does not treat energetic plasma in the inner magnetosphere properly, the increase in temperature implies an increased source density of energetic particles which may then start to drift into the inner magnetosphere.

Besides B_z and the temperature, v_x and E_y also show clear signatures at the onset times. However, the time series of v_x and E_y show the onset as a brief spike as compared to the B_z and the temperature. In particular, v_x and E_y reach their particular maxima at the AL_s index onset time while they start an already significant increase before the onset in the AL_s index occurs. This is most evident in the second substorm at 385 min where E_y and v_x increase about 10 min before the AL_s index shows any change.

The question that arises is at which point in the tail substorm signatures do occur first. We have compared time series at x = -8 R_E (shown here), x = -12 R_E, and x = -20 R_E (not shown here). Unfortunately, no conclusions can be drawn from these comparisons. Some of the signatures occur

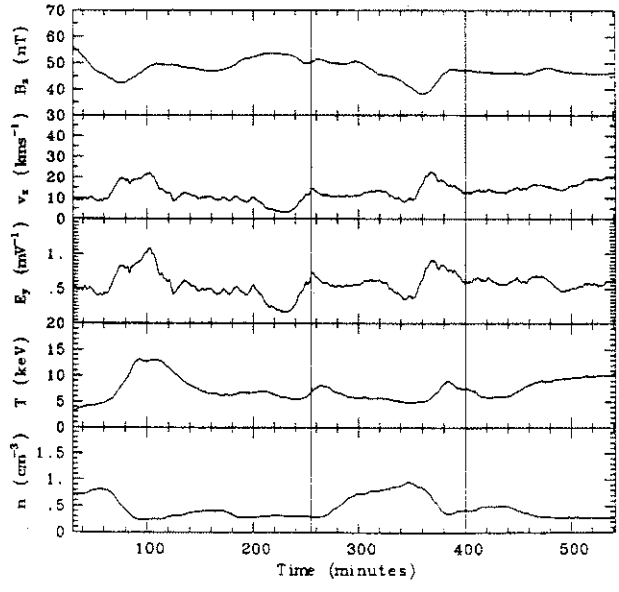

Fig. 5. Time series ("virtual spacecraft observation") of B_z, v_x, E_y, temperature, and number density at (-8 R_E,0 R_E, 0 R_E) for run #2.

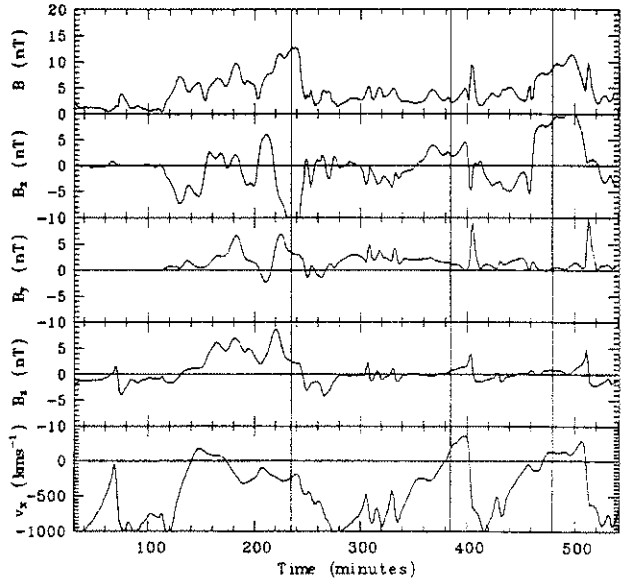

Fig. 6. Time series ("virtual spacecraft observation") of B, B_x, B_y, B_z, and v_x in the distant tail plasma sheet at (-100 R_E,0 R_E,0 R_E) for run #1.

virtually simultaneously within the accuracy limit of about ±3 minutes. For instance, this is the case for the field dipolarization and the temperature increase of the first substorm at -8 and -12 R_E. Other signatures are not conclusive. For example, at the second substorm the field starts to dipolarize at -12 R_E, 10 minutes before it starts to dipolarize at -8 R_E. The temperature increase occurs simultaneously at both locations, and the spike in E_y occurs first at -8 R_E and about 10 minutes later at -12 R_E. Obviously, we need to study more cases, use better time and spatial resolution, and develop better analysis techniques to determine the exact onset location and the physical processes that cause the onset.

Figure 5 shows the same quantities as Figure 4 but for the weakly forced case (run #2). In this case there are clear substorm expansion onsets in the AL_s index at 255 min and 400 min. Unlike in the previous case, however, substorm signatures in the tail are either very weak or totally absent. There is no apparent increase in B_z for the first substorm, and the signatures in v_x, E_y and the temperature are very weak. The second substorm shows clearer signatures, but the dipolarization and the temperature increase start 35 minutes before there are any signatures in the AL_s index. As in the strongly forced case, the increase in v_x and E_y precedes the field dipolarization.

To conclude the analysis of the two simulation runs we examine the substorm signatures in the distant tail. We have placed two virtual spacecraft at (-100 R_E, 0 R_E, 0 R_E) and at (-100 R_E, 0 R_E, 12 R_E) to simulate measurements taken in the plasma sheet and in the lobes, respectively. Figure 6 shows B, B_x, B_y, B_z, and v_x in the plasma sheet and Figure 7 the same quantities in the northern lobe. We first note in Figure 6 that the plasma sheet B_z turns southward at 245 min, 10 minutes after the AL_s onset. However, the B_z signature is not that typical of a plasmoid [Baker et al., 1987], which would require an increase in B_z before the southward

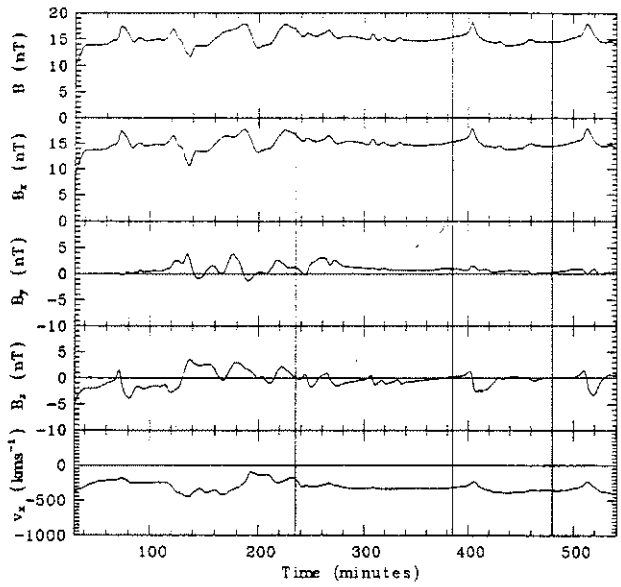

Fig. 7. Time series ("virtual spacecraft observation") of B, B_x, B_y, B_z, and v_x in the distant tail northern lobe at (-100 R_E,0 R_E,12 R_E) for run #1.

turn. Inspection of the tail field topology (not shown here) reveals that the tail field is closed well beyond -100 R_E before the substorm onset. Thus the virtual spacecraft cannot observe the head of the plasmoid because it is already past the spacecraft when it is formed. It does see, however, the O-line (the southward turning of the field) which develops well earthward of the spacecraft. The other two substorms have clear signatures of a passing plasmoid in the distant tail associated with them. The passage of these plasmoids (centered at 405 min and 515 min) is marked by the dipolar signature in B_z, a strong B_y core field, and the onset of strong tailward flows of up to 1000 km s^{-1}. There are some smaller events between 300 and 350 min and around 425 min. While these events would not readily be identified as plasmoids from the time series shown here, inspection of the field topology shows that these events are indeed small plasmoids which are about 20 R_E long and a few R_E thick. For all of the aforementioned plasma sheet signatures we find corresponding signatures in the lobes. In Figure 7 two major traveling compression regions (TCRs) can be identified at 405 min and 515 min by their characteristic dipolar signature in B_z and their peaks in B. They are coincident with the bipolar B_z signatures of the plasmoid in the plasma sheet. Smaller TCRs can be seen at 310, 320, 335, 430 and 460 min, and each of them is associated with a small plasmoid. The first substorm onset does not have a TCR signature associated with it, but a rather gradual decrease of the total field that starts before the AL_s index onset time at 225 min and ends at 310 min when a series of 3 small TCRs begins. Again, this can be understood by the formation of a large plasmoid and the ensuing unloading of the tail.

The distant tail signatures of the weakly forced case (not shown here) are mostly similar to the strongly forced case, but appear much less pronounced. One major difference is that we do not find any large plasmoids that would correspond to the second and third onset in the strongly forced case. Instead, we find signatures of a series of small plasmoids, both in the plasma sheet and in the lobes. A detailed analysis of the differences in the tail dynamics between the two cases requires the examination of the three-dimensional structure of the tail and will be presented elsewhere.

4. Summary and Conclusion

We have presented two global MHD simulation cases with the same IMF sequence but different solar wind plasma parameters in order to investigate the relation between the solar wind and geomagnetic activity. The first and most important finding is that our simulation model can reproduce most of the commonly observed signatures of geomagnetic activity, and of substorms in particular, both in the ionosphere and in the tail. This is particularly evident in the case of strong solar wind forcing. We can clearly identify the sudden decrease in the AL_s index, field dipolarization and the onset of earthward flows in the near-Earth tail, and the signatures of plasmoids in the distant tail. Another substorm signature that we find in the simulation is the increase of the plasma temperature in the near-Earth tail. This temperature increase may be related to the particle injection events into the inner magnetosphere that are commonly observed near or at substorm expansion phase onset. As for the ionospheric and ground signatures we have concentrated on the AL and AU indices because they are extensively used in substorm studies. Although the model also provides more detailed ionospheric parameters, such as currents, conductances, and some characteristics of electron precipitation, which may be used to infer the auroral luminosity, we defer the analysis of these to a later publication and do not discuss them here.

Comparing the two simulation runs we find that the activity in the AL_s and AU_s indices is not solely controlled by the IMF, but that the solar wind density and velocity, or related quantities like E_y or the dynamic pressure, also play a prominent role. There is considerable activity in the AL_s and AU_s indices when the solar wind dynamic pressure is high and IMF has no southward component. Also, after the IMF turns southward, the substorm signatures are stronger and more pronounced when the solar wind dynamic pressure is high. One should keep in mind, however, that the AL_s and AU_s indices that we use in this study are different from the actual AU and AL indices. The latter are derived from only a few ground stations (typically 12) and do not provide much coverage. The synthetic AU_s (AL_s) have a much wider coverage, particularly in latitude, and therefore reflect the true maximum of the eastward (westward) electrojets more closely. Because of the limited coverage, the AL and AU indices are not only sensitive to the maximum electrojet current, but also to its location. Therefore, the activity that we find during nothward IMF and strong solar wind forcing may not appear in AL and AU if the electrojets are too far north of the stations. With the weak solar wind forcing, on the other hand, we find that the AL_s and AU_s indices reach very low values which implies that the electrojets are weak everywhere in the auroral latitudes.

The activity in the tail also varies, depending on the solar wind forcing. With strong forcing we find all of the substorm tail signatures that can be derived from the MHD simulation. However, when the solar wind dynamic pressure is

weak some of the substorm signatures may be absent or not very pronounced and difficult to identify. For instance, the substorm (in AL_s) ensuing after the southward turning of the IMF does not show any field dipolarization in the near-Earth tail. Because of these weak or absent tail signatures, the events that we have termed substorms in the weakly forced case may not be identified as substorms if data from only the tail are taken into account. Considering that the real AL index has only limited coverage and may miss some of the onsets that we see in the AL_s , the southward IMF interval in the weakly forced case may be called a SMC (steady magnetic convection) event. One may speculate that there is a transition from strong to weak forcing where substorm signatures disappear and the magnetosphere enters a mode of steady convection. A related question is whether the substorms can be classified into different types with different signatures or whether instead there is a continous spectrum of substorms with gradual changes of signatures. Obviously, two simulation runs are not sufficient and we need to cover a wider range of solar wind parameters to answer these questions.

Finally, comparison of the IMF with the AL_s and AU_s indices indicates that the geomagnetic activity has both a driven and a spontaneous component. The substorms following the southward turning of the IMF are clearly driven. On the other hand, the activity during the following southward interval is spontaneous since there are no triggers in the solar wind.

Acknowledgements. This research is supported by NASA grant NAGW-1100 at UCLA. Computations were carried out on the Intel Paragon at the San Diego Supercomputer Center.

References

Baker, D. N., S.-I. Akasofu, W. Baumjohann, J. W. Bieber, D. H. Fairfield, E. W. Hones, B. H. Mauk, R. L. McPherron, and T. E. Moore, Substorms in the magnetosphere, In *Solar Terrestrial Physics – Present and Future*, edited by D. M. Butler and K. Papadopoulos, NASA Ref. Pub. 1120, 1984.

Baker, D. N., S. J. Bame, D. J. McComas, R. D. Zwickl, J. A. Slavin, and E. J. Smith, Plasma and magnetic field variations in the distant magnetotail associated with near-earth substorm effects, in *Magnetotail Physics*, edited by A. T. Y. Lui, The John Hopkins University Press, Baltimore, 1987.

Bargatze, L. F., D. N. Baker, R. L. McPherron, and E. W. Hones, Magnetospheric impulse response for many levels of geomagnetic activity, *J. Geophys. Res.*, *90*, 6387, 1985.

Borovski, J. E., R. J. Nemzek, and R. D. Belian, The occurrence rate of magnetospheric substorm onsets: Random and periodic substorms, *J. Geophys. Res.*, *98*, 3807, 1993.

Brecht, S. H., J. G. Lyon, J. A. Fedder, and K. Hain, A time dependent three dimensional simulation of the Earth's magnetosphere: reconnection events *J. Geophys. Res.*, *87*, 6098, 1982.

Evans, C. R., and J. F. Hawley, Simulation of magnetohydrodynamic flows: A constrained transport method, *Ap. J.*, *332*, 659, 1988.

Fedder, J. A., and J. G. Lyon, The solar wind – magnetosphere – ionosphere current – voltage relationship, *Geophys. Res. Lett.*, *14*, 880, 1987.

Hardy, D. A., M. S. Gussenhoven, R. Raistrick, and W. J. McNeil, Statistical and functional representations of the pattern of auroral energy flux, number flux, and coductivity, *J. Geophys. Res.*, *92*, 12275, 1987.

Harten, A., and G. Zwas, Self-adjusting hybrid schemes for shock computations, *J. Comp. Phys.*, *9*, 568, 1972.

Hirsch, C., *Numerical Computation of Internal and External Flows*, Volume II, Wiley, New York, 1990.

Hoshino, M., and A. Nishida, Numerical simulation of the dayside reconnection, *J. Geophys. Res.*, *88*, 6926, 1983.

Kamide, T., and S. Matsushita, Simulation studies of ionospheric electric fields and currents in relation to field aligned currents, 1, Quiet periods, *J. Geophys. Res.*, *84*, 4083, 1979.

Kamide, Y., The relationship between field-aligned currents and the auroral electrojets: A review, *Space Sci. Rev.*, *31*, 127, 1982.

Lopez, R. E., and A. T. Y. Lui, A multisatellite study of the expansion of a substorm current wedge in the near-Earth magnetotail, *J. Geophys. Res.*, *95*, 8009, 1990.

Lui, A. T. Y., R. E. Lopez, S. M. Krimigis, R. W. McEntire, L. J. Zanetti, and T. A. Potemra, A case study of magnetotail current sheet disruption and diversion, *Geophys. Res. - Lett.*, *15*, 721, 1988.

Lyons, L. R., D. S. Evans, and R. Lundin, An observed relation between magnetic field aligned electric fields and downward electron energy fluxes in the vicinity of auroral forms, *J. Geophys. Res.*, *84*, 457, 1979.

McPherron, R. L., Physical processes producing magnetospheric substorms and magnetic storms, *Geomagnetism*, *4*, 593, 1990.

Moen, J., and A. Brekke, The solar flux influence on quiet time conductances in the auroral ionosphere, *Geophys. Res. - Lett.*, *20*, 971, 1993.

Moldwin, M. B., and W. J. Hughes, Geomagnetic substorm association of plasmoids, *J. Geophys. Res.*, *98*, 81, 1993.

Ogino, T., A three dimensional MHD simulation of the interaction of the solar wind with the Earth's magnetosphere: The generation of field aligned currents, *J. Geophys. Res.*, *91*, 6791, 1986.

Ohtani, S., S. Kokubun, and C. T. Russell, Radial expansion of the tail current disruption during substorms: A new approach to the substorm onset region, *J. Geophys. Res.*, *97*, 3129, 1992.

Pytte, T., R. L. McPherron, E. W. Hones, and H. I. West, Jr., Multiple satelite studies of magnetospheric substorms: Distinction between polar magnetic substorms and convection driven negative bays, *J. Geophys. Res.*, *83*, 663, 1978.

Sergeev, V. A., and W. Lennartsson, Plasma sheet at $X \approx -20R_E$ during steady magnetospheric convection, *Planet. Space Sci.*, *36*, 353, 1988.

Slavin, J. A., D. N. Baker, J. D. Craven, R. C. Elphic, D. H. Fairfield, L. A. Frank, A. B. Galvin, W. J. Hughes, R. H. Manka, D. G. Mitchell, I. G. Richardson, T. R. Sanderson, D. G. Sibeck, E. J. Smith, and R. D. Zwickl, CDAW 8 observations of plasmoid signatures in the geomagnetic tail: An assessment, *J. Geophys. Res.*, *94*, 15153, 1989.

Slavin, J. A., M. F. Smith, E. L. Mazur, D. N. Baker, T. Iyemori, H. J. Singer, and E. W. Greenstadt, ISEE-3 plasmoid and TCR observations during an extended interval of substorm activity, *Geophys. Res. Lett.*, *19*, 825, 1992.

Takahashi, K., L. J. Zanetti, R. E. Lopez, R. W. McEntire, T. A. Potemra, and K. Yumoto, Disruption of the magnetotail current sheet observed by AMPTE/CCE, *Geophys. Res. Lett.*, *14*, 1019, 1987.

Walker, R. J., T. Ogino, J. Raeder, and M. Ashour-Abdalla, A global magnetohydrodynamic simulation of the magnetosphere when the interplanetary magnetic field is southward: The onset of magnetotail reconnection, *J. Geophys. Res.*, *98*, 17235, 1993.

Watanabe, K., and T. Sato, Global simulation of the solar wind – magnetosphere interaction: The importance of its numerical validity, *J. Geophys. Res.*, *95*, 75, 1990.

Yahnin, A., M. V. Malkov, V. A. Sergeev, R. J. Pellinen, O. Aulamo, S. Vennerström, E. Friis-Christensen, K. Lassen, C. Danielsen, J. D. Craven, C. Deehr, and L. A. Frank, Features of steady magnetospheric convection, *J. Geophys. Res.*, *99*, 4039, 1994.